Near-Infrared Plasmonic 2D Semimetals for Applications in Communication and Biology

*Zhengfeng Zhu, Yousheng Zou, Weida Hu, Yuebin Li, Yu Gu, Bingqiang Cao, Nan Guo, Lin Wang, Jizhong Song, Shengli Zhang, Haoshuang Gu, and Haibo Zeng**

Localized surface plasmon resonance (LSPR) has many applications which require meeting specific wavelength windows. The most prominent examples are photothermal therapy in biology, matched to the biological window (650–1350 nm), and communication relying on photodetection in optoelectronics, matched to the communication window (1260–1675 nm). However, for the classic noble metals (Au, Ag), tuning LSPRs from visible region to these two windows is still a demanding task due to their intrinsic limitations on charge density and dielectric function. Here, the discovery of near-infrared biological and communication window-matched plasmonic properties of semimetal TiS_2 nanosheets (NSs) is reported for the first time. Developed synthesis procedures allow fine-tuning width and thickness of single-crystal TiS_2 NSs. During characterization a new and intensive absorption peak in the 1000–1400 nm range is observed from both TiS_2 NS colloid solutions and films. This peak is attributed to LSPR due to its dependence on particle shape and on the refractive index of solvents. The superiority of such LSPRs is demonstrated in both, biological and optical applications: excitation at 808 and 980 nm generates a ≈50 °C photothermal temperature rise, while excitation at 1310 nm results in two-times enhanced photocurrents of PbS photodetectors compared to untreated devices.

1. Introduction

Localized surface plasmon resonance (LSPR), the collective electron oscillation excited by light, was first discovered in 1902[1], and then recognized as a universal characteristic of various metallic nanoparticles.[2–4] From then on, plasmonics has evoked considerable attentions due to its rich scientific connotation as well as its potential applications in various fields.[5–7] Especially, LSPRs exhibit enhanced near-field amplitude with high localization and spatial resolution at the resonant wavelength, which is widely used to enhance the performance of biological imaging,[8] photothermal therapy,[9] and optoelectronic devices,[10,11] etc.

However, the practical applications to the biological and photoelectric fields have been limited to the utilization of expensive noble metals including Ag,[12] Au,[13] etc., for decades. The LSPRs of colloidal suspension of Ag and Au nanopsheres in water locate approximately at 400 and 500 nm. For both materials, the resonances are difficult to redshift to the biological (650–1350 nm) and communication (1260–1675 nm) windows.[14,15] The current strategy to tune the resonant wavelength relies on complicated and elaborate adjustments on microstructures, such as nanorods,[9,16] nanocages,[17] and nanoshells.[18] Even though, the tunability is still very limited, e.g., the LSPRs wavelength of Au can only be tuned near 700–1000 nm using such complicated manipulation of particle shape.

Here, for the first time, we report the discovery of biological and communication windows-matched LSPRs of semimetal TiS_2 nanosheets (NSs), and their robust plasmonic effects on temperature rise of photothermal therapy and detection enhancement of NIR photodetectors. The TiS_2 NSs were found to exhibit a novel and intensive absorption peak in the range of 1000–1400 nm, besides the inherent interband absorption peak near 700 nm. The experimental observation of its dependence on particle shape and refractive index of the solvent, as well as finite difference time domain (FDTD) simulations confirmed that the newly observed NIR absorption peak originates from the LSPR of TiS_2 NSs. The superiority of such NIR LSPRs was demonstrated by ≈50 °C photothermal temperature rise under excitations with wavelength 808 and 980 nm (in biological

Dr. Z. Zhu, Prof. Y. Zou, Prof. Y. Gu, Prof. J. Song, Prof. S. Zhang, Prof. H. Zeng
Institute of Optoelectronics and Nanomaterials
Jiangsu Key Laboratory of Advanced Micro and Nano Materials and Technology
College of Material Science and Engineering
Nanjing University of Science and Technology
Nanjing 210094, China
E-mail: zeng.haibo@njust.edu.cn
Prof. W. Hu, Dr. N. Guo
National Laboratory for Infrared Physics
Shanghai Institute of Technical Physics
Chinese Academy of Sciences
500 Yu Tian Road, Shanghai 200083, China
Prof. Y. Li, Dr. L. Wang, Prof. H. Gu
Collaborative Innovation Center for Advanced Organic Chemical Materials and Faculty of Physics and Electronic Science
Hubei University
Wuhan 430062, China
Prof. B. Cao
School of Material Science and Engineering
University of Jinan
Jinan 250022, China

DOI: 10.1002/adfm.201504884

© 2016 WILEY-VCH Verlag GmbH & Co. KGaA, Weinheim

window), and by the more than two times enhancement of photocurrents of PbS photodetectors under excitations of 1310 nm (in communication window). Such NIR LSPRs from semimetal nanomaterials could open up a new group of materials toward biological and communication-functional plasmonics.

2. Results and Discussion

2.1. Concept of Near-Infrared Plasmon from 2D Semimetal

LSPRs are collective electron charge oscillations in metallic nanoparticles that are excited by incident light. According to its basic definitions, several factors are necessary to activate LSPR from a nanoparticle, especially the sufficiently high concentration of free charges as well as sufficiently small size of particles compared to the resonant wavelength to provide a strong charge confinement. The resonant wavelength for a given material is mainly determined by its dielectric function $\varepsilon(\omega)$, its shape, and the permittivity of medium ε_m. If we apply a simple Drude model for $\varepsilon(\omega)$ without considering damping effects and assume a spherical shape of the particle, the resonant frequency can be described by Equation (1), where N is the concentration of free electrons, m_e is the effective mass of free carrier, e is the charge of one electron, and ε_∞ is the high-frequency permittivity of the material

$$\omega_{sp} = \sqrt{Ne^2/(\varepsilon_0 m_e(\varepsilon_\infty + 2\varepsilon_m))} \quad (1)$$

Based on equation (1), the resonant wavelength $\lambda_{sp} = 2\pi c/\omega_{sp}$ (c: speed of light in vacuum) is inversely proportional to $N^{1/2}$. As a result, materials with free electron concentration more than 10^{22} cm^{-3} is required to have the resonance in the visible range ($\lambda_{sp} < 700$ nm). This is why the noble metal nanoparticles have been the focus of nanoplasmonics for a long time.[3,4] For a typical spherical Au nanoparticle in water, its resonant wavelength locates at 500 nm as shown in **Figure 1**. Recently, LSPRs were also observed in the heavily doped semiconductor nanocrystals with their charge density as high as 10^{21} cm^{-3}.[19]

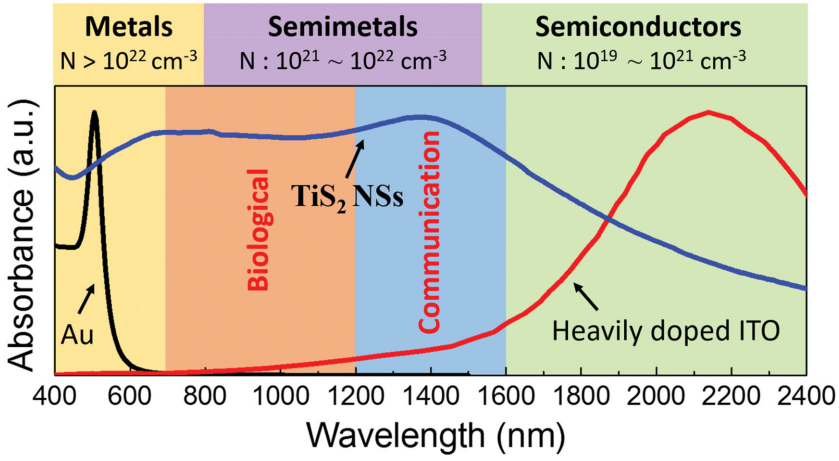

Figure 1. Characteristics of NIR LSPR from semimetal. General dependence of the LSPR wavelength on free carrier concentrations (N) for metal, semimetal, and heavily doped semiconductors.

However, none of the resonant wavelengths fit the Near-Infrared (NIR) biological and communication windows.[20–23] According to equation (1), if $N = 10^{21}$ cm^{-3} and $\varepsilon_\infty + 2\varepsilon_m = 5$, the resonant wavelength is about 2 μm. Therefore, a new group of materials with LSPR located in NIR waveband covering the biological and communication windows is yet to be found. Besides noble metals and heavily doped semiconductors, semimetals are also able to provide sufficiently high-charge concentrations for LSPRs. Moreover, their charge densities can be in the range ≈10^{21}–10^{22} cm^{-3}, between those of metals and semiconductors. Based on equation (1), such carrier density could induce LSPRs located right in the biological and communication windows.[24] The experimental absorption spectrum of titanium disulfide NS (a typical semimetal) also confirms this statement as shown in Figure 1.

From a structure perspective, the semimetal TiS_2 has several advantages to be a promising candidates for NIR LSPR in the biological and communication windows. First, TiS_2 has a typical layered structure with weak van der Waals interactions between (001) planes as shown in **Figure 2**a, rendering the c dimension reducible from a bulk size into nanometer even atomic scale through bottom up or top down method. Such shrink in c axis could provide strong confinement of charge to induce longitudinal LSPRs. Second, as shown by the energy band structure calculated by density functional theory (DFT) in Figure 2b, there is an apparent overlap of valence band and conduction band, indicating its semimetallic characteristic of TiS_2 which possesses sufficient free carrier concentrations (≈10^{20} cm^{-3}) in bulk TiS_2[25] and the concentration can be as high as 10^{23} cm^{-3} for the ultrathin 2D layered structure.[26]

2.2. Elaborate Controls on Width and Thickness of 2D TiS_2 Nanosheets

The single-crystal TiS_2 nanosheets were prepared via modified colloidal chemistry method, which is similar to previous reports.[27] Briefly, $TiCl_4$ and CS_2 were selected as Ti and S precursors, mixed, and then heated in the mixed solvent of oleylamine (OAm) and octadecen (ODE) at 300 °C for 3 h. OAm acted as the growth solvent, while ODE as the protecting agent. Here, the width and thickness are finely controlled according to the adjustment of temperature and ODE concentration.

As the scanning electron microscope (SEM) image shown in **Figure 3**a, the products are TiS_2 NSs with very uniform morphology and narrow size distribution, the large production and corresponding size distribution can be seen from the full SEM image presented in Figure S1 in the Supporting Information. Moreover, Figure 3b,c are the low-resolution transmission electron microscope (TEM) images both from top and side-view, confirming their uniform hexagonal morphology and equal thickness of obtained TiS_2 NSs, which is necessary for the study of the LSPR characteristic

© 2016 WILEY-VCH Verlag GmbH & Co. KGaA, Weinheim

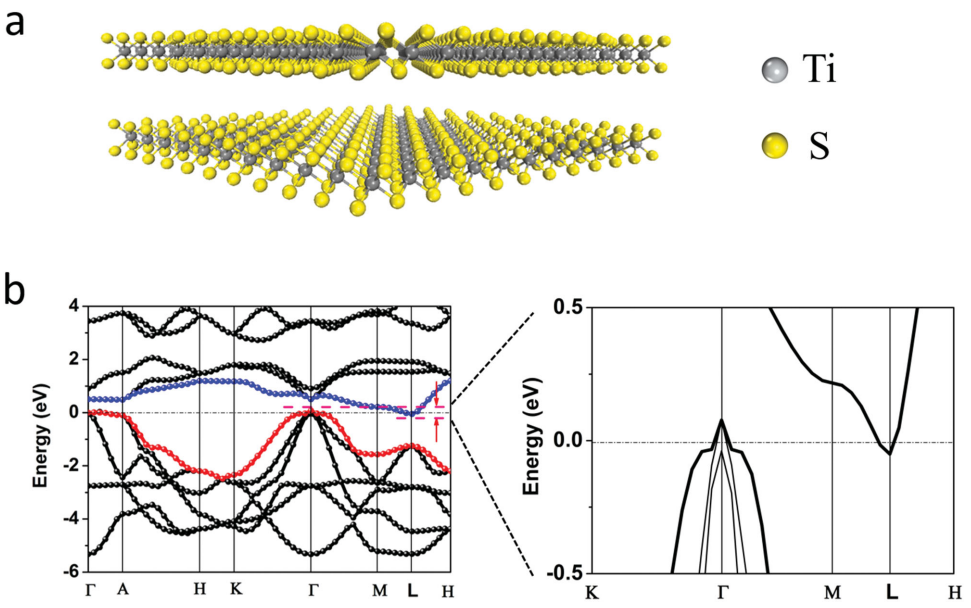

Figure 2. Crystal and band structure of TiS_2. a) Visualization of TiS_2 using a ball and stick model to illustrate the 2D layered structure. b) Calculated energy band structure of 2D TiS_2 by density function theory, indicating the semimetal characteristics.

of a nanomaterial. Then, the highly hexagonal crystal facet in Figure 3d is its (001) plane of TiS_2 with the corresponding (110), (100) interplanar spacings (as shown in Figure 2d) of 1.7 and 2.9 Å, respectively. Figure 3e exhibits its layered structure of a NS with an interplanar spacing of 0.57 nm, consistent with its theoretical interlayer spacing, and the corresponding

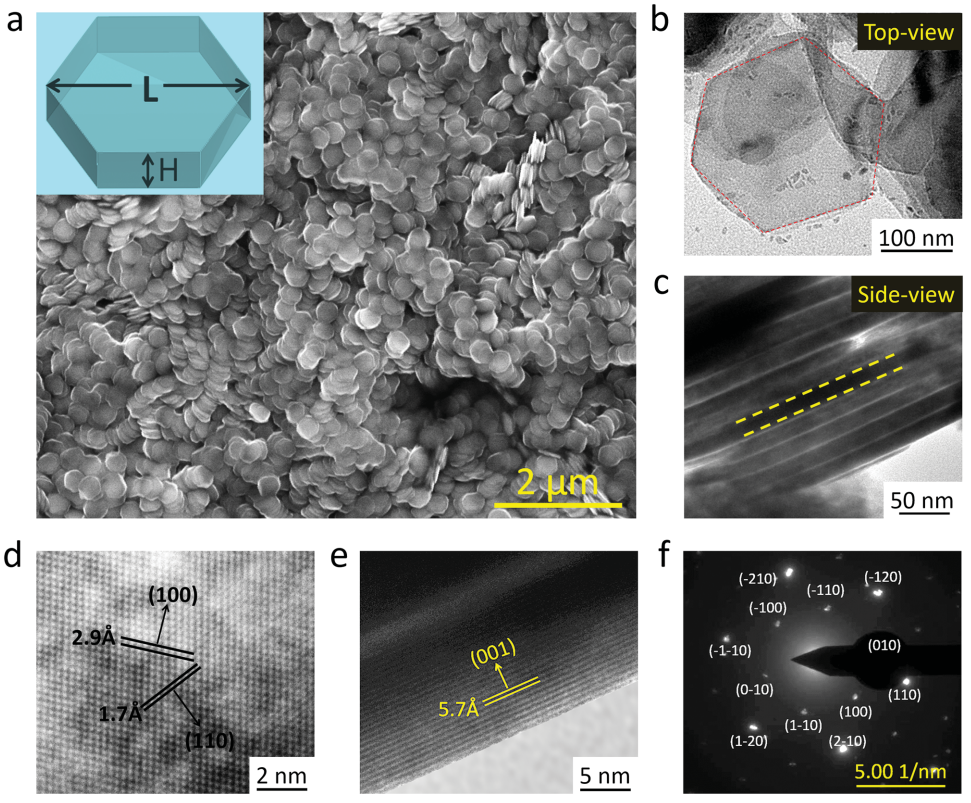

Figure 3. a) SEM images of TiS_2 NSs, inset shows the 3D morphology of a single TiS_2 NS, the size and thickness of which are defined as L and H, respectively. b) Top-view and c) side-view low-resolution TEM images of TiS_2 NSs. d,e) Corresponding top-view and side-view high-resolution TEM images. f) Detailed selected area electron diffraction (SAED) of a single TiS_2 NS.

© 2016 WILEY-VCH Verlag GmbH & Co. KGaA, Weinheim

selected area electron diffraction of a single TiS_2 NS is presented in Figure 3f, indicating its hexagonal phase of TiS_2 NS. More importantly, as their X-ray diffraction (XRD) pattern (**Figure 4**b) and EDXS spectrum (Figure S2, Supporting Information) of obtained TiS_2 NSs show, they are very pure in phase without any oxide and particle by-products, which frequently appeared in previous reports.[28] All these features confirm the single-crystal characteristics of the obtained TiS_2 NSs with a typical lateral size (L) of ≈300 nm and thickness (H) of ≈16 nm (the definition of L and H are presented in the inset of Figure 3a). Hence, such ultrathin NSs provide strong confinement of the charges and single crystal structures ensure the high mobility which is required for the strong collective oscillation of LSPRs.

Varying reactant concentration, nucleation rates and growth rates, the structural parameters, H and L, can be well controlled. For examples, both L and H will decrease with the increase of reactant concentration, while only L deceases when prolonging nucleation time. Therefore, a series of TiS_2 NSs with different H and L can be obtained as shown in **Figure 5**, and their detailed correspondences of H and L are presented in Figure S3 in the Supporting Information. Meanwhile, the crystallinity of obtained TiS_2 NSs with short reaction time for 1 h is poor than that with longer time, as observed from the XRD pattern in Figure 4c, and the TEM of inset can also confirm its amorphous edge of TiS_2 NS obtained with short time. Subsequently, the capability of accurate shape and size control allows us to do the subsequent study of the geometrical dependence of LSPRs.

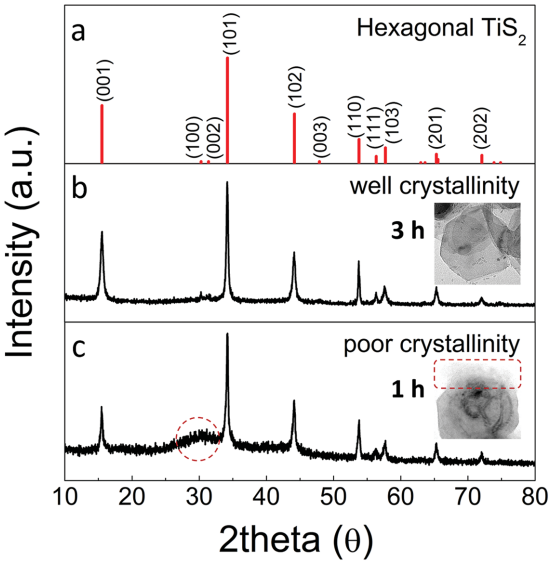

Figure 4. X-ray diffraction (XRD) powder pattern for obtained TiS_2 NSs. a) Joint Committee on Powder Diffraction Standards powder pattern no. 15-0853 for hexagonal (P-3 mL) TiS_2. b,c) XRD powder pattern of TiS_2 NSs with well and poor crystallinity, reacted for 3 and 1 h when prepared, respectively, insets show the corresponding TEM images. TiS_2 NSs with poor crystallinity are obtained when the reaction time is relatively short, reflected in the amorphous edges, mainly corresponding to the lattice plane of (100) and (002).

2.3. Characteristics of LSPRs from TiS_2 Nanosheets

The UV–vis–NIR absorption spectra of semimetal TiS_2 NSs are studied in **Figure 6**. The distinct spectra difference of bulk TiS_2 from its nanostructured counterpoints can be observed from Figure 6a. The absorption of bulk TiS_2 or poorly crystalline TiS_2 NSs only shows a sharp peak at 570 nm, marked as "A" band, which comes from the interband transitions from chalcogen p states to Ti 3d states according to our DFT calculations and previous reports[29–31] However, for the single-crystal TiS_2 NSs, a new absorption peak at 1380 nm emerges, marked as "B", which has never been observed before. Meanwhile, B band is so strong that it distorts A band significantly and results in a shoulder over the whole range of ≈600–1600 nm, perfectly covering the optical windows for both biological and communication applications.

Such newly observed B band can be attributed to LSPR of semimetal TiS_2 NSs according to the following facts. First, the measured B band can be well fitted by the simulated spectrum using FDTD calculations as shown in Figure 6a, and the detailed fitting process is described as follows. In the simulation, the permittivity of TiS_2 is described by equation (1) by using the free electron Drude model, and the simulations are restricted to be starting from 1200 nm to avoid large disturbance from the interband transition

$$\varepsilon(\omega) = 1 - \frac{\omega_p^2}{\omega(\omega + i\gamma)} \tag{2}$$

To simulate the full spectrum (from 400 to 2400 nm), additional terms correspond to Lorentz oscillators should be added to equation (1) to account for the interband transition. Since our main focus is to uncover the underlying physics of peak B, we would like to stick to the much simpler Durde model and only study the long wavelength band (>1200 nm) where the contribution of the interband transition is weak.

For the permittivity of the material described by equation (1), both plasma frequency ω_p and collision frequency γ are unknowns and are taken as adjustable parameters. Peak position is mainly determined by ω_p and peak width is determined by γ. Since the nanosheets are oriented randomly in the solution, we considered three different cases for each simulation, case I: $\boldsymbol{k}\perp\boldsymbol{n}$, $\boldsymbol{E}//\boldsymbol{n}$, case II: $\boldsymbol{k}\perp\boldsymbol{n}$, $\boldsymbol{E}\perp\boldsymbol{n}$, case III: $\boldsymbol{k}//\boldsymbol{n}$, $\boldsymbol{E}\perp\boldsymbol{n}$ (Figure 6b). $\boldsymbol{k}$ is the wave vector of the plane wave, E is the electric component of the electromagnetic wave, and $\boldsymbol{n}$ is the normal vector of the particle surface. For each case, the extinction cross section is calculated and denoted as σ_I, σ_{II}, σ_{III}, respectively. Figure 6b indicates that the peak only appears in case I where the E-field is perpendicular to the particle surface. The extinction cross section to compare with experimental data is the average of these three different cases

$$\bar{\sigma} = (\sigma_I + \sigma_{II} + \sigma_{III})/3 \tag{3}$$

By adjusting both ω_p and γ, the averaged extinction cross section can be matched to the experimental data as shown in Figure 6c, the peak profile at the long wavelength side show excellent agreement with experimental result. It is a direct evidence that a simple Drude model is sufficient to describe the optical properties of TiS_2 in this waveband and peak B can be attributed to LSPR.

© 2016 WILEY-VCH Verlag GmbH & Co. KGaA, Weinheim

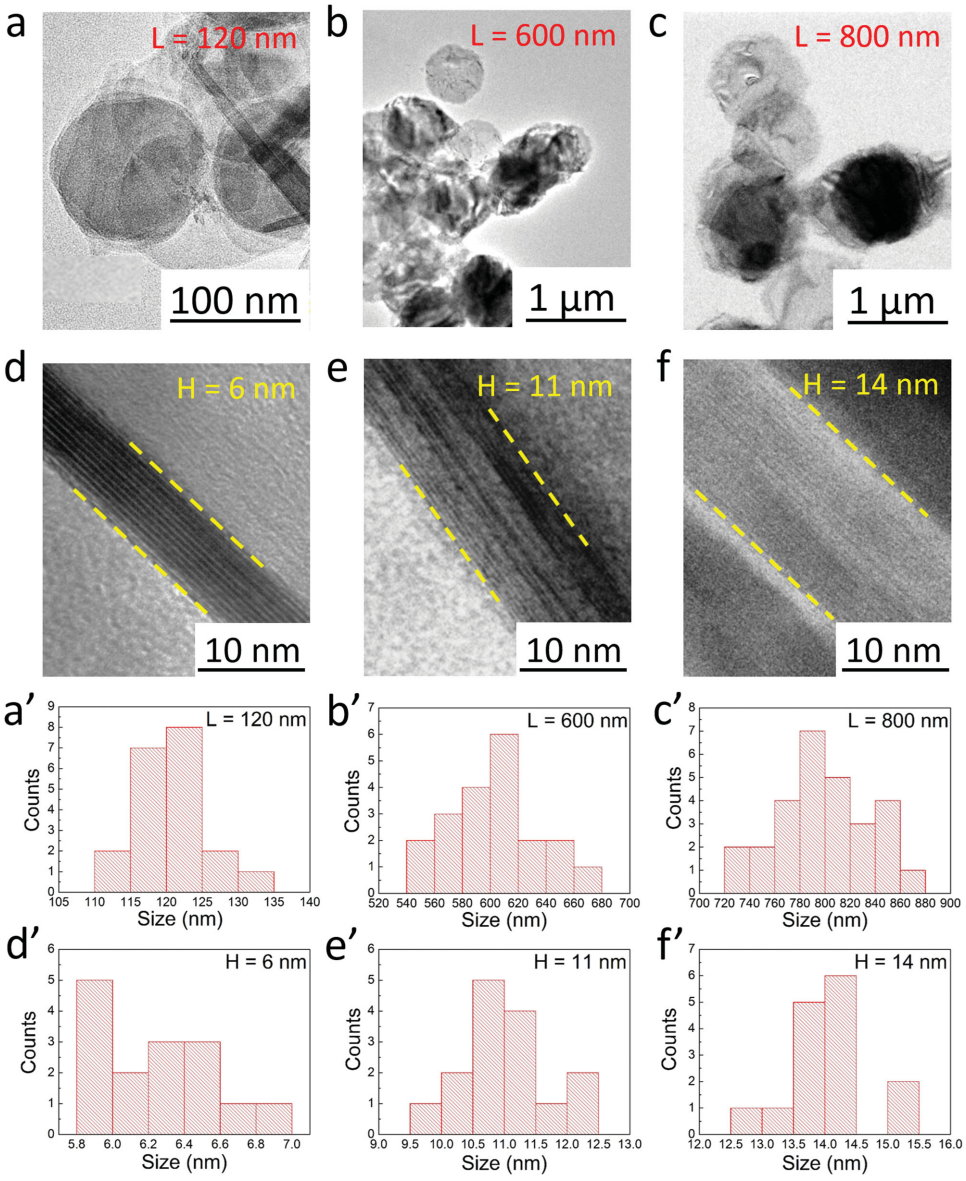

Figure 5. Controlled fabrication of semimetal TiS_2 NSs. a–c) Low-resolution TEM images of TiS_2 NSs with different plane size of 120, 600, and 800 nm. d–f) Low-resolution TEM images of TiS_2 NSs with different thickness of 6, 11, and 14 nm. Panels (a′–f′) are their corresponding size distribution of panels (a–f).

To further prove the assigning of peak B to LSPR, we studied the evolutions of B band with the surrounding medium and geometrical parameters of the particle. As shown in Figure 6d, the B band experiences a gradual redshift when the medium refractive index is increasing: 1.46 (CCl_4), 1.51 (C_2Cl_4), and 1.63 (CS_2), consistent with the unique regularity of equation (1), as the characteristic from the LSPRs. Moreover, the B band shifts toward long wavelength with the increase of thickness as shown in **Figure 7**a, which is extremely size-dependent. These tendencies are the precise trademarks of LSPR and can be explained by using Mie scattering theory for an oblate ellipsoid.[32,33]

Using the fitting parameters obtained from Figure 6b, the corresponding absorption spectrums are directly simulated (ω_p is fixed and some minor adjustment on γ is allowed), and all of the evolutions can be well fitted by FDTD simulations except for the 6 nm thick sample (Figure 7a). This is probably due to the additional scattering caused by the particle surface limiting the mean free path of the electrons.[34,35] Hence, a greater damping effect than the other samples is expected resulting in a weaker and broader peak. The LSPR peak for the 6 nm thick sample is comparable with the absorption edge of A band for the 6 nm sample. Therefore, the simple Durde model is not sufficient to account for the contributions from both A and B bands. This also explains the insensitive lateral size dependence for the 6 nm thick sample as shown in Figure 7b. The resonance is strongly damped by scattering from the particle surface so that the expected shift of resonance is immersed in

© 2016 WILEY-VCH Verlag GmbH & Co. KGaA, Weinheim

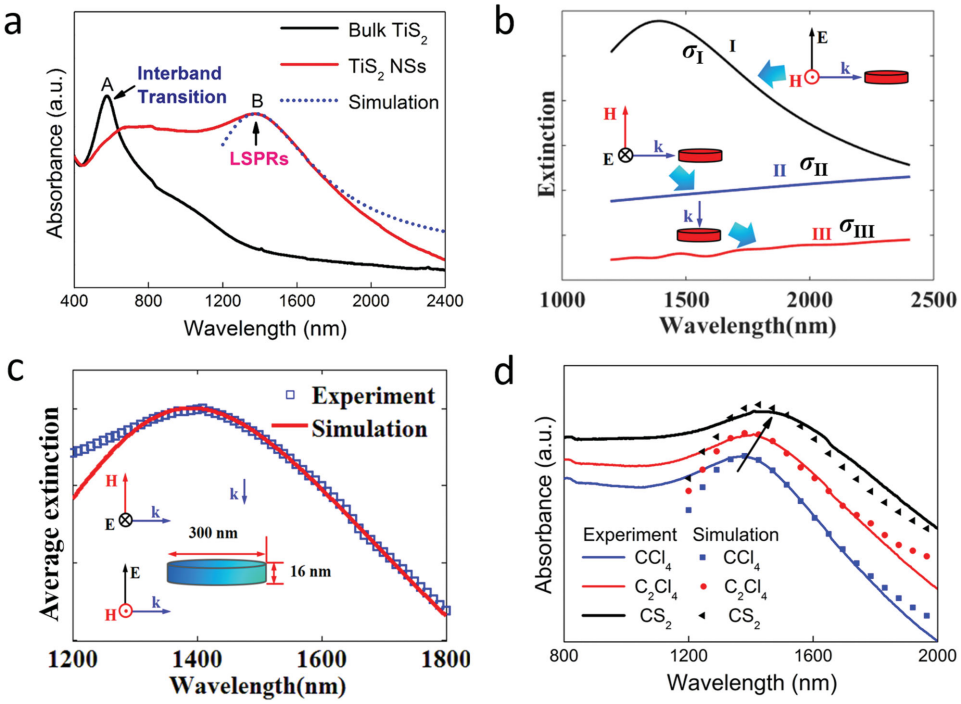

Figure 6. Characteristics of the LSPRs from TiS_2 NSs. a) UV–vis–NIR absorption spectra of bulk and TiS_2 NSs. b) FDTD simulation extinction spectrum for three different cases. In case I, the *E*-vector is perpendicular to the surface of TiS_2 nanosheet. In Case II and III, the *E*-vector is parallel to the surface of TiS_2 nanosheet. c) Fitting of the simulating results with the experimental data. In this simulation, the size $L = 300$ nm, height $H = 16$ nm. Plasma frequency $\omega_p = 1.56 \times 10^{15}$ rad s^{-1}, collision frequency $\gamma = 7 \times 10^{14}$ rad s^{-1}. After ω_p and γ are found for one particular simulation, ω_p will be fixed for the later simulation and only some minor adjustments of γ will be allowed to get better fit. d) Absorption spectra of TiS_2 NSs in different surrounding media. The refractive indices of CCl_4, C_2Cl_4, and CS_2 are 1.46, 1.51, and 1.63, respectively. Solid lines are experimental data and dotted lines are FDTD simulations.

the absorption edge of A band and the LSPR peak cannot be observed apparently.

2.4. Application of LSPRs on Photodetectors at Communication Window

Obviously, one of the merits of LSPR is the near-field enhancement effect at the resonant wavelength, which has been widely applied to enhance the performances of bioimaging, photocatalysis, photodetection, etc.[36–38] Here, the natural NIR LSPR of semimetal TiS_2 NSs offers great opportunities for the applications in both biological technology and optic communication as demonstrated subsequently.

Figure 8a presents the device configuration of a NIR photodetector with PbS quantum dots (QDs) as photoresponsive medium and inserted TiS_2 NSs as plasmonic enhancement layer, which works at the 1310 nm communication wavelength. To spin coat a homogeneous TiS_2 layer loading PbS QDs, the TiS_2 NSs were composited with polymethyl methacrylate

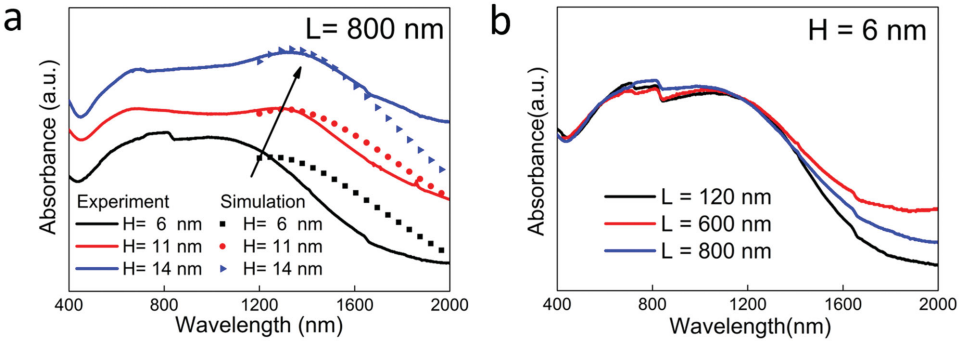

Figure 7. Size dependence of LSPRs from TiS_2 NSs. a) Absorption spectra of TiS_2 NSs with different thickness and fixed planar sizes of 800 nm. b) Absorption spectra of TiS_2 with different planar sizes and fixed thickness of about 6 nm. Solid lines are experimental data and dotted lines are FDTD simulations.

© 2016 WILEY-VCH Verlag GmbH & Co. KGaA, Weinheim

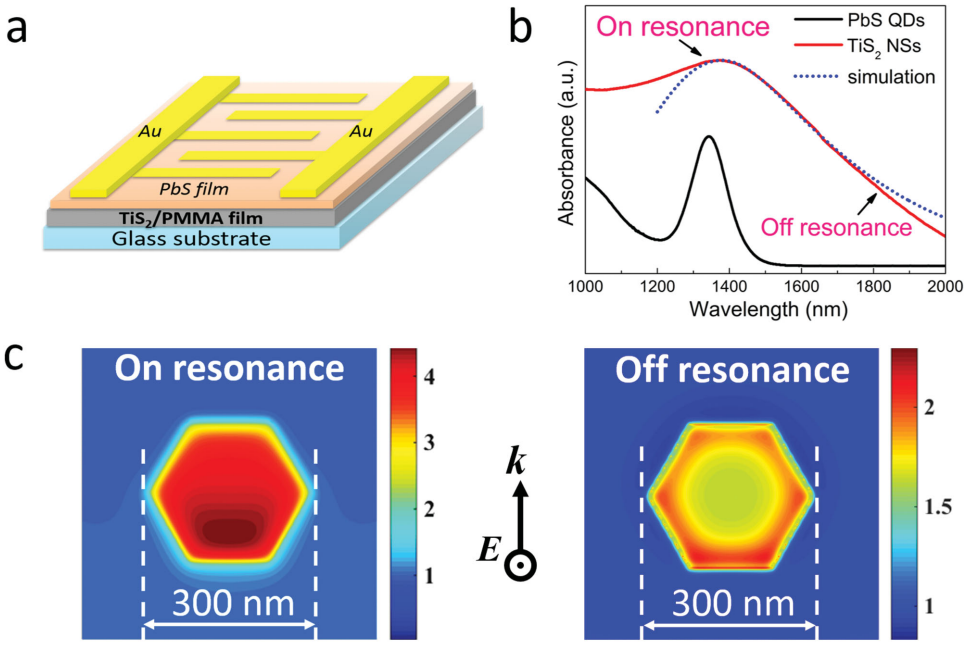

Figure 8. a) Schematics of photodetector configuration with TiS_2 NSs as plasmonic enhancing layer. b) Comparison of absorption spectrum of PbS photoconductive layer and TiS_2 NSs. c) Corresponding E-field distribution for a TiS_2 NS ($L = 300$ nm, $H = 16$ nm) at the wavelength of 1380 and 1800 nm, respectively.

(PMMA), but not weaken their inherent LSPRs characteristics too much (as presented in Figure S6 in the Supporting Information). Figure 8b shows the absorption spectrum of the adopted QDs, exhibiting a characteristic excitonic peak at 1350 nm, the corresponding size of which is 4.6 nm showed in Figure S4 in the Supporting Information. The comparison clearly demonstrates the perfect matching between excitonic absorption and LSPR of TiS_2 NS, which ensures the strong near field enhancement inside the photodetector devices. The near field enhancement is clearly depicted by the FDTD simulation results in Figure 8c, where the E-field enhancement effect is very strong when excited by ≈1200–1500 nm light, while relatively weak under irradiation of 1800 nm light.

Such near field enhancement will lead to the elevation of photocurrent as shown in **Figure 9**a, which is a net current resulted from the illumination. The excitation source is a 1310 nm laser, and the powers are 2.5, 4.5, 6, 8, and 10 mW, respectively. In comparison with the simple device, the photocurrents of photodetectors with TiS_2 layer are enhanced to 2.3, 2.4, 2.4, 2.6, and 2.7 times, respectively. The irradiance-dependent responsivity is also about twice as high as that of the simple device without TiS_2 as shown in Figure 9b. The near field enhancement demonstrated here could have significant potentials in NIR optical communication and imaging applications.

2.5. Application of LSPRs on Photothermal Therapy at Biological Window

Furthermore, besides the photodetection in communication wavelength, the near-field amplitude enhancement effect due to the LSPRs of TiS_2 NSs can also be applied to photothermal

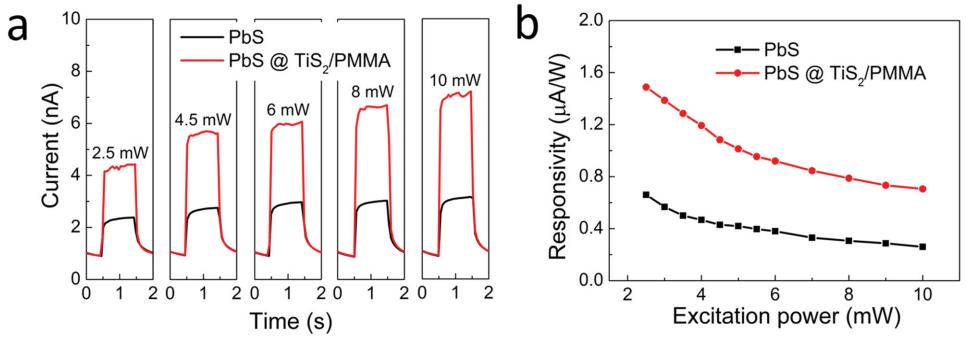

Figure 9. Plasmonic enhancement on photodetection. a) Current–time (I–t) curves of photodetectors with and without TiS_2 NSs layer under illumination with different power (2.5, 4.5, 6, 8, 10 mW). b) Dependence of the responsivity on illumination power for photodetectors with and without 2D TiS_2 layer, respectively.

© 2016 WILEY-VCH Verlag GmbH & Co. KGaA, Weinheim

therapy at wavelength within the biological window. Though relative work was reported that TiS_2 NSs were successfully applied for in vivo photoacoustic imaging and photothermal,[39] but the previous work cannot clearly explain the mechanism of the photothermal effect. Hence, it is necessary for us to demonstrate this effect precisely resulting from the LSPRs of TiS_2 NSs via a new experimental system different from the previous one in this work. **Figure 10**a shows the schematic diagram of photothermal therapy using TiS_2 NSs. Under a low-energy NIR illumination, intense absorption of photons by the TiS_2 NSs arising from LSPR will increase the temperature of surrounding cancer cells and inactivate them gradually without damaging the non-cancer cells.

In order to adapt for the biological aqueous environment, the hydrophobic TiS_2 NSs were assembled with F127 to form hydrophilic F127/TiS_2 composite micelles for the photothermal application. The photographs of F127/TiS_2 composite micelles water solution with different concentration shown in Figure 10b and the F127/TiS_2 composite micelles exhibit wonderful hydrophilicity, which can be steadily dispersed in water but not in either chloroform or *n*-hexane (Figure S7, Supporting Information). Meanwhile, the average hydraulic size of nanomicelles is 190 nm (Figure 10c), slightly larger than the average size of pure TiS_2 NSs, which is attributed to the extension of polyethylene oxide (PEO) block in water. As shown in Figure 10d, a negative zeta potential of −10 mV could further provide static repulsion to enhance the aqueous stability of as-prepared TiS_2/F127 composite nanomicelles.

Figure 11 exhibits their corresponding characteristic photothermal temperature rise behavior with different concentration of F127/TiS_2 under 808 and 980 nm laser irradiation, and the irradiation power are 0.5 and 1 W with corresponding energy density of 0.64 and 1.27 W cm^{-2}, respectively. The laser power and wavelength are selected to optimize the photothermal heating effect. Similar temperature rise is obtained both under the 808 and 980 nm, and the maximum temperature rise can be as high as 50 °C. More importantly, the strong temperature rise clearly demonstrates that the photothermal effect is from TiS_2 NSs due to their NIR LSPRs, successfully confirming the mechanism of photothermal attributed to the LSPRs of TiS_2 NSs. Moreover, with the low toxicity of TiS_2 NSs to cells,[39] they have significant potentials in photothermal therapy of cancer cells.

TiS_2 NS obtained in this work can successfully apply in NIR wavelength due to its strong localized surface plasmon resonances (LSPSs), it can effectively replace noble metal Au with the advantages of low cost and easy synthesis when applied for photothermal therapy. Meanwhile, it is a rare material with NIR LSPRs successfully used for enhancing the NIR photodetection. However, when used for these related applications, more other improvements can be done, such as treating the surface of NSs to heighten their dispersibility and optimizing the TiS_2 film to improve the properties of E-field enhancement.

3. Conclusion

High-quality hexagonal TiS_2 NSs with high crystallinity and purity are successfully synthesized. Characterization of the material reveals a hitherto elusive absorption peak in the 1000–1400 nm range. This peak exhibits a characteristic bathochromic shift that increases with both the refractive index of the surrounding solvent and also with the thickness of the nanosheet. Experimental evidence and FDTD simulations

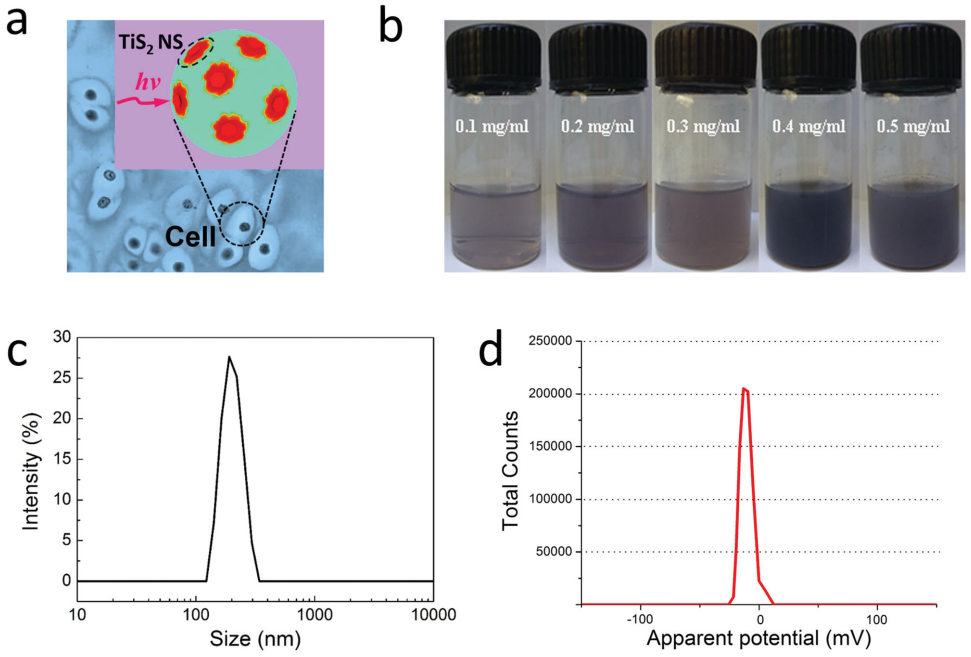

Figure 10. Surface modification of TiS_2 NSs. a) Schematic diagram of the heating effects of TiS_2 NSs aiming at cancer cells in biological tissue. b) Photographs of F127/TiS_2 composite micelles dispersed in water with different concentration under the sunlight. c) The hydraulic size of TiS_2/F127 nanomicelles. d) The zeta potential of TiS_2 NSs of TiS_2/F127 nanomicelles.

© 2016 WILEY-VCH Verlag GmbH & Co. KGaA, Weinheim

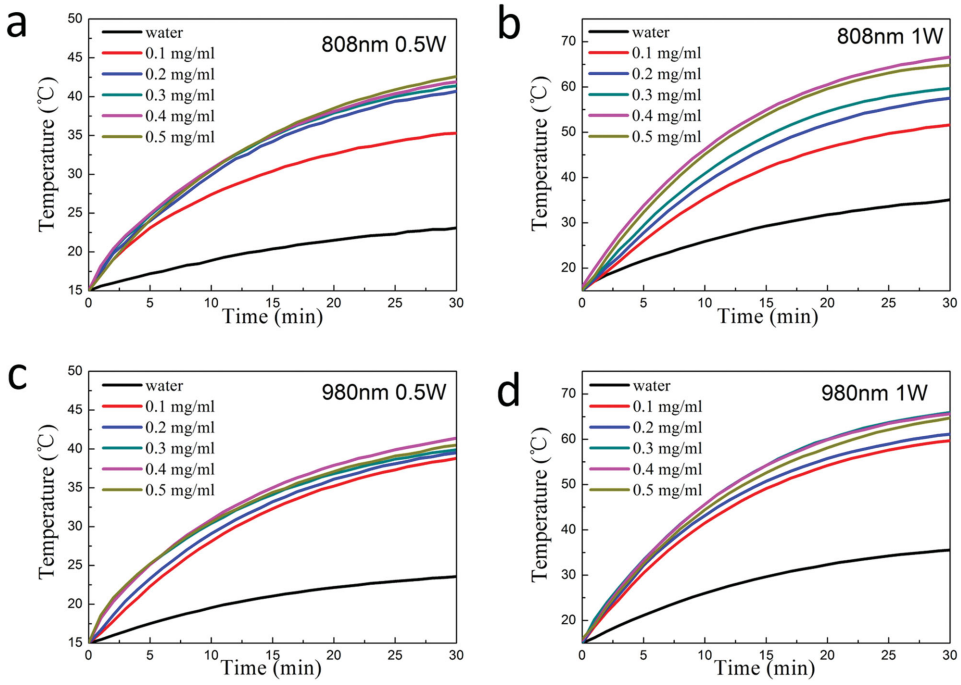

Figure 11. Plasmonic photothermal effect. Temperature evolution curve of F127/TiS_2 composite micelles with varied concentration from 0.1, 0.2, 0.3, 0.4 to 0.5 mg mL^{-1}, under different laser irradiation in 30 min. The irradiation wavelength and power of the used laser are a) 808 nm, 0.5 W, 0.64 W cm^{-2}, b) 808 nm, 1 W,1.27 W cm^{-2}, c) 980 nm, 0.5 W, 0.64 W cm^{-2}, and d) 980 nm, 1 W, 1.27 W cm^{-2}.

attribute this peak to LSPRs, rendering the TiS_2 NSs synthesized in this work the first semimetal with NIR LSPR properties. By using different irradiation wavelengths applications of this effect are successfully demonstrated in technical and biological settings. Under 1310 nm illumination, photocurrents recorded by PbS photodetectors coated with TiS_2 NSs are enhanced by more than 100% compared to uncoated devices. Irradiation under 980 nm, however, causes an extraordinary temperature rise of about 50 °C due to LSPRs, which can be applied to kill cancer cells. In summary TiS_2 NSs show great potentia by constituting the first semimetal material amenable to general plasmonics applications in the NIR regime.

4. Experimental Section

Synthesis of TiS_2 NSs: In a typical procedure, 0.1 mmol titanium chloride ($TiCl_4$, 99.99%, Aladdin-reagent) was mixed with 11.2 mmol oleylamine (J&K chemical) and 15 mL octadecene (>90%(GC), Aladdin-reagent) in a 100 mL four-neck flask with strong magnetic stirring, heated to a low-boiling temperature and excluding air and impurities with high-purity argon for several times. After removing impurities, the reaction mixture was heated to 220 °C for 30 min under Ar conditions. Subsequently, carbon disulfide (CS_2, AR, Aladdin-reagent) was injected into the mixture and reaction temperature was heated to 300 °C ultimately. After 3 h, the reaction was quenched and cooled down to room temperature quickly. By addition of 10 mL butanol into the black solutions, TiS_2 NSs were precipitated via centrifugation and redispersed in hexane, then the sample was washed twice with ethanol by centrifugation.

Synthesis of the PbS Colloidal Quantum Dots (CQDs): 0.9 g lead (II) oxide, 2.7 mL oleic acid, 1 mL oleylamine, and 15 mL 1-octadecene were added in a three-neck flask, evacuated for 10 min to remove air and impurities with low boiling point, then heated to 160 °C keeping for 40 min. After 0.1 mL CS_2 was injected to the mixture and reacted for 5 s, the reaction was stopped and cooled down to the room temperature immediately. Products were precipitated by acetone and washed three times, then redispersed in toluene to prepare a 30 mg mL^{-1} solution ready for device fabrication.

Device Fabrication: First, TiS_2/PMMA was prepared by TiS_2 NSs (100 mg) mixed with poly(methyl methacrylate) (3 g) in chloroform (10 mL) and stirred for 2 h. Then, the PbS film was deposited by spin-coating the ready PbS CQDs toluene solution onto glass substrate with or without TiS_2/PMMA film covered at 2000 rpm for 30 s, respectively. The ligand exchange was then carried out by covering the former film with three drops of 10% (v/v in methanol) mercaptopropionic acid (MPA), which was repeated two times every 5 s. Sequentially, the film was rinsed three times with five drops of methanol to remove the residual MPA. After the above sequence repeated another two times, the film was heated at 90 °C for 10 min on the heating panel. Finally, the interdigitated Au electrodes were deposited on the film by thermal evaporation utilizing a shadow mask.

Material Characterization: The optical extinction spectra of TiS_2 NS suspensions were measured by a Shimadzu UV-3600 UV–Vis–NIR spectrophotometer (in the 250–3300 nm spectral range). TEM images were taken on a TECNAI G2 20 LaB6 TEM instrument operated at an acceleration voltage of 200 kV. XRD patterns were acquired using a Bruker D8 Advance X-ray diffractometer operating with Cu Kα radiation (λ = 1.5406 Å). Surface SEM images of the NSs were obtained on a Quant 250 FEG SEM instrument.

Photoelectronic Measurements: The measurement was carried out by a probe station connected to Keithley 4200-SCS semiconductor characterization system. Illumination was controlled at 1310 nm generated from laser diodes (Thorlabs SFL1550S).

Photothermal Measurements: The light source was provided by 808 and 980 nm wavelength semiconductor laser device (Beijing STONE Laser Co. LTD, P. R. of China) whose power could be adjusted externally (≈0–8 W). The temperature was recorded by an online type thermocouple thermometer (XMT 8008 Yuyao Tenghui Thermostat Factory, China) every 1 min.

© 2016 WILEY-VCH Verlag GmbH & Co. KGaA, Weinheim

Supporting Information

Supporting Information is available from the Wiley Online Library or from the author.

Acknowledgements

Z.Z., Y.Z., W.H., Y.L., Y.G., and B.C. contributed equally to this work. This work was financially supported by the National Key Basic Research Program of China (Grant No. 2014CB931702), NSFC (Grant Nos. 51572128, 51173038, and 51303046), NSFC-RGC (Grant No. 5151101197), and the PAPD of Jiangsu Higher Education Institutions.

Received: November 14, 2015
Revised: December 2, 2015
Published online: January 22, 2016

[1] R. W. Wood, *Proc. Phys. Soc., London* **1902**, *18*, 269.
[2] J. A. Creighton, D. G. Eadon, *J. Chem. Soc., Faraday Trans.* **1991**, *87*, 3881.
[3] P. K. Jain, X. H. Huang, I. H. El-Sayed, M. A. El-Sayed, *Acc. Chem. Res.* **2008**, *41*, 1578.
[4] Y. K. Mishra, R. Adelung, G. Kumar, M. Elbahri, S. Mohapatra, R. Singhal, A. Tripathi, D. K. Avasthi, *Plasmonics* **2013**, *8*, 811.
[5] Y. K. Mishra, S. Mohapatra, R. Singhal, D. K. Avasthi, D. C. Agarwal, S. B. Ogale, *Appl. Phys. Lett.* **2008**, *92*, 043107.
[6] Z. T. Li, Z. N. Zhu, W. J. Liu, Y. L. Zhou, B. Han, Y. Gao, Z. Y. Tang, *J. Am. Chem. Soc.* **2012**, *134*, 3322.
[7] Y. T. Li, J. L. Tang, L. C. He, Y. Liu, Y. L. Liu, C. Y. Chen, Z. Y. Tang, *Adv. Mater.* **2015**, *27*, 4075.
[8] I. H. El-Sayed, X. H. Huang, M. A. El-Sayed, *Nano Lett.* **2005**, *5*, 829.
[9] X. H. Huang, I. H. El-Sayed, W. Qian, M. A. El-Sayed, *J. Am. Chem. Soc.* **2006**, *128*, 2115.
[10] H. A. Atwater, A. Polman, *Nat. Mater.* **2010**, *9*, 205.
[11] X. Liu, L. C. He, J. Z. Zheng, J. Guo, F. Bi, X. Ma, K. Zhao, Y. L. Liu, R. Song, Z. Y. Tang, *Adv. Mater.* **2015**, *27*, 3273.
[12] S. D. Solomon, M. Bahadory, A. V. Jeyarajasingam, S. A. Rutkowsky, C. Boritz, L. Mulfinger, *J. Chem. Educ.* **2007**, *84*, 322.
[13] S. Link, *J. Phys. Chem. B* **1999**, *103*, 4212.
[14] A. M. Smith, M. C. Mancini, S. M. Nie, *Nat. Nanotechnol.* **2009**, *4*, 710.
[15] E. H. Sargent, *Adv. Mater.* **2005**, *17*, 515.
[16] Z. N. Zhu, J. Guo, W. J. Liu, Z. T. Li, B. Han, W. Zhang, Z. Y. Tang, *Angew. Chem., Int. Ed.* **2013**, *52*, 13571.
[17] W. Hasan, C. L. Stender, M. H. Lee, C. L. Nehl, J. Lee, T. W. Odom, *Nano Lett.* **2009**, *9*, 1555.
[18] C. Loo, A. Lowery, N. J. Halas, J. West, R. Drezek, *Nano Lett.* **2005**, *5*, 709.
[19] K. Manthiram, A. P. Alivisatos, *J. Am. Chem. Soc.* **2012**, *134*, 3995.
[20] M. Kanehara, H. Koike, T. Yoshinaga, T. Teranishi, *J. Am. Chem. Soc.* **2009**, *131*, 17736.
[21] J. A. Faucheaux, P. K. Jain, *J. Phys. Chem. Lett.* **2013**, *4*, 3024.
[22] I. Kriegel, C. Y. Jiang, J. Rodriguez-Fernandez, R. D. Schaller, D. V. Talapin, E. da Como, J. Feldmann, *J. Am. Chem. Soc.* **2012**, *134*, 1583.
[23] T. R. Gordon, T. Paik, D. R. Klein, G. V. Naik, H. Caglayan, A. Boltasseva, C. B. Murray, *Nano Lett.* **2013**, *13*, 2857.
[24] J. M. Luther, P. K. Jain, T. Ewers, A. P. Alivisatos, *Nat. Mater.* **2011**, *10*, 361.
[25] E. Guilmeau, Y. Bréard, A. Maignan, *Appl. Phys. Lett.* **2011**, *99*, 052107.
[26] C. W. Lin, X. J. Zhu, J. Feng, C. Z. Wu, S. L. Hu, J. Peng, Y. Q. Guo, L. L. Peng, J. Y. Zhao, J. L. Huang, J. L. Yang, Y. Xie, *J. Am. Chem. Soc.* **2013**, *135*, 5144.
[27] S. Jeong, D. Yoo, J. T. Jang, M. Kim, J. Cheon, *J. Am. Chem. Soc.* **2012**, *134*, 18233.
[28] V. V. Plashnitsa, F. Vietmeyer, N. Petchsang, P. Tongying, T. H. Kosel, M. Kuno, *J. Phys. Chem. Lett.* **2012**, *3*, 1554.
[29] F. R. Shepherd, P. M. Williams, *J. Phys. C: Solid State Phys.* **1974**, *7*, 4416.
[30] S. C. Bayliss, W. Y. Liang, *J. Phys. C: Solid State Phys.* **1985**, *18*, 3327.
[31] A. H. Reshak, S. Auluck, *Phys. Rev. B* **2003**, *68*, 245113.
[32] G. Mie, *Ann. Phys.* **1908**, *25*, 337.
[33] K. L. Kelly, E. Coronado, L. L. Zhao, G. C. Schatz, *J. Phys. Chem. B* **2003**, *107*, 668.
[34] S. Link, M. A. El-Sayed, *Int. Rev. Phys. Chem.* **2000**, *19*, 409.
[35] S. A. Maier, *Plasmonics: Fundamentals and Applications*, Springer Science & Business Media, New York, **2007**.
[36] B. Qin, H. Y. Chen, H. Liang, L. Fu, X. F. Liu, X. H. Qiu, S. Q. Liu, R. Song, Z. Y. Tang, *J. Am. Chem. Soc.* **2010**, *132*, 2886.
[37] P. K. Jain, K. Manthiram, J. H. Engel, S. L. White, J. A. Faucheaux, A. P. Alivisatos, *Angew. Chem. Int. Ed.* **2013**, *52*, 13671.
[38] L. B. Luo, L. H. Zeng, C. Xie, Y. Q. Yu, F. X. Liang, C. Y. Wu, L. Wang, J. G. Hu, *Sci. Rep.* **2014**, *4*, 3914.
[39] X. Qian, S. Shen, T. Liu, L. Cheng, Z. Liu, *Nanoscale* **2015**, *7*, 6380.

© 2016 WILEY-VCH Verlag GmbH & Co. KGaA, Weinheim